Bol. Soc. Paran. Mat.
©SPM – E-ISSN-2175-1188
SPM: www.spm.uem.br/bspm

(3s.) **v. 2025 (43) 3** : 1–18.
ISSN-0037-8712
doi:10.5269/bspm.78735

Boundary Layer Analysis of MHD Heat and Mass Transfer with Soret and Dufour Effects on a Wedge Surface

Vanaja K.* and Chenna Sumalatha

ABSTRACT: This study investigates the influence of magnetohydrodynamics (MHD), Soret (thermal diffusion), and Dufour (diffusion-thermo) effects on heat and mass transfer in an electrically conducting nanofluid flow past a wedge. The governing equations for momentum, energy, and species transport are derived from first principles and transformed into a system of nonlinear ordinary differential equations through similarity transformations. These equations are solved numerically using a Runge–Kutta-based shooting technique. The findings indicate that increasing the magnetic parameter suppresses velocity while enhancing thermal and concentration boundary layers. The Soret effect elevates concentration distributions, whereas the Dufour effect increases the thermal field, demonstrating strong cross-diffusion coupling. The Prandtl and Schmidt numbers were found to control the thinning of thermal and solutal boundary layers, respectively. A comparison of the present numerical results with previously reported benchmark solutions shows excellent agreement, validating the accuracy of the method and extending earlier studies by incorporating coupled MHD, Soret, and Dufour effects.

Key Words: MHD, wedge surface, soret and Dufour effects.

Contents

1. Introduction

Boundary-layer flows over wedges, commonly referred to as Falkner–Skan type flows, have received considerable attention due to their broad engineering and industrial applications. Such flows arise naturally in aerodynamic heating of aerospace vehicles, chemical reactors, turbine blade cooling, extrusion processes, and nuclear engineering systems, where fluid motion over wedge-shaped geometries plays a critical role in determining the transport of heat and mass. The classic works of Blasius and Falkner–Skan established the theoretical foundation for wedge flows, providing similarity transformations that reduce the governing equations to tractable boundary-value problems. Since then, researchers have extended

* Corresponding author.
2010 *Mathematics Subject Classification:* 35B40, 35L70.
Submitted September 09, 2025. Published October 07, 2025

these formulations to include variable fluid properties, porous media, and non-linear effects relevant to practical scenarios.

The presence of a magnetic field further enriches the problem. In conducting fluids, magnetohydrodynamic (MHD) forces introduce a Lorentz force that modifies the velocity field, suppresses instabilities, and alters both momentum and thermal transport. This has practical importance in MHD power generation, metallurgical processing, polymer extrusion, and plasma physics, where flow control under electromagnetic fields is often desirable. Moreover, MHD effects in nanofluids have been shown to yield controllable heat and mass transfer enhancement, making the subject particularly attractive for modern high-performance applications.

Another important consideration is the role of cross-diffusion phenomena, namely the Soret (thermal-diffusion) and Dufour (diffusion-thermo) effects. These effects become non-negligible in multicomponent systems with steep temperature and concentration gradients, such as in chemical and geophysical flows. The Soret effect induces mass flux driven by temperature gradients, while the Dufour effect introduces an additional energy flux due to concentration gradients. These mechanisms significantly alter the coupling between heat and mass transfer processes and are essential in accurately modeling separation processes, isotope diffusion, combustion, and porous media transport. Their inclusion in MHD wedge flows with nanofluids thus provides a more realistic description of transport phenomena.

The study of boundary layer flows and associated heat and mass transfer phenomena has remained a cornerstone in fluid mechanics and engineering applications. The pioneering works of Blasius [16] and Falkner–Skan [1,18] laid the foundation for boundary layer theory, providing analytical and approximate solutions to flow over flat plates and wedge geometries. Subsequent advancements, including the computational methods by Cebeci and Keller [19], have enabled deeper exploration of nonlinear boundary layer problems.

In many practical applications, such as in metallurgy, geothermal engineering, and cooling of nuclear reactors, the presence of a magnetic field significantly alters the transport characteristics of electrically conducting fluids. Magnetohydrodynamic (MHD) boundary layer flows have therefore attracted extensive attention [3,6,7,8,10,11,12]. The magnetic parameter introduces the Lorentz force, which suppresses fluid motion and modifies velocity, temperature, and concentration profiles, thereby affecting both heat and mass transfer.

The coupling of heat and mass transfer through cross-diffusion effects, namely the Soret (thermal diffusion) and Dufour (diffusion-thermo) effects, has been recognized as an important mechanism in multicomponent systems. Gebhart and Pera [13] were among the first to analyze the combined buoyancy effects of heat and mass diffusion. Postelnicu [4] and Cheng [5] further demonstrated that these cross-diffusion phenomena significantly influence natural convection in porous media. More recently, Alam et al. [21] and Gautam et al. [22] have extended the analysis of Soret and Dufour effects in MHD flows, highlighting their importance in modern thermal and mass transfer processes.

The role of variable physical properties and boundary conditions, such as temperature-dependent viscosity [14], radiation effects [9], and non-uniform heating [20], has also been extensively investigated. These studies have established the sensitivity of heat and mass transfer rates to physical parameters, offering pathways to optimize thermal management in industrial systems. Furthermore, the introduction of nanofluids [2,11,23] has opened new avenues in enhancing transport processes due to improved effective conductivity and diffusivity.

Particular attention has also been given to wedge geometries, which serve as generalized cases between flat plate and stagnation point flows. Srinivasacharya et al. [23] examined MHD nanofluid flows over a wedge, demonstrating the crucial influence of wedge angle on boundary layer characteristics. Such configurations are of practical importance in aerospace engineering, turbine blade cooling, and polymer extrusion processes.

Motivated by the above, the present work investigates boundary-layer flow over a wedge surface under the combined influence of MHD forces, Soret and Dufour effects. A mathematical model is formulated from the governing conservation equations of mass, momentum, energy, and species diffusion, incorporating appropriate similarity transformations to reduce the system to coupled, nonlinear ordinary differential equations. These equations are solved numerically using a shooting technique based on the fourth-order Runge–Kutta (RK4) method, which ensures accuracy and stability in capturing the flow, thermal, and

concentration fields. The analysis highlights the influence of magnetic parameter, wedge angle, Prandtl number, Schmidt number, Soret number, and Dufour number on velocity, temperature, and concentration distributions, as well as on the associated local Nusselt and Sherwood numbers. The findings are expected to contribute both to theoretical development and to practical optimization of heat and mass transfer in electrically conducting nanofluid systems.

2. Mathematical Modeling

Let $\mathbf{V}$ be the velocity, p the pressure, T the temperature and C the species concentration. For an incompressible, Newtonian, electrically conducting fluid in a transverse magnetic field $\mathbf{B}$, the governing equations are:

Continuity (incompressible):

$$\nabla \cdot \mathbf{V} = 0. \tag{2.1}$$

Momentum (Navier–Stokes with Lorentz force, quasi-static MHD):.

$$\rho\left(\frac{\partial \mathbf{V}}{\partial t} + \mathbf{V}\cdot\nabla\mathbf{V}\right) = -\nabla p + \mu\nabla^2\mathbf{V} + \rho\mathbf{g} + \mathbf{J}\times\mathbf{B}, \tag{2.2}$$

where under the low magnetic Reynolds number (quasi-static) assumption $\mathbf{J} \approx \sigma(\mathbf{V}\times\mathbf{B})$ and the Lorentz force may be modeled in boundary-layer form as a linear drag in the streamwise direction:

$$\mathbf{J}\times\mathbf{B} \approx -\sigma B^2(\mathbf{V} - \mathbf{U}_e),$$

with $\mathbf{U}_e$ the free-stream velocity. Thus we will use:

$$\rho\left(\frac{\partial \mathbf{V}}{\partial t} + \mathbf{V}\cdot\nabla\mathbf{V}\right) = -\nabla p + \mu\nabla^2\mathbf{V} - \sigma B^2(\mathbf{V} - \mathbf{U}_e) + \rho\mathbf{g}. \tag{2.3}$$

Energy (including Dufour effect):

$$\rho c_p\left(\frac{\partial T}{\partial t} + \mathbf{V}\cdot\nabla T\right) = k\nabla^2 T + D_f\nabla^2 C, \tag{2.4}$$

where D_f denotes the effective Dufour coefficient (diffusion–thermo coupling).

Species (including Soret effect):

$$\frac{\partial C}{\partial t} + \mathbf{V}\cdot\nabla C = D_B\nabla^2 C + \frac{D_t}{T_\infty}\nabla^2 T, \tag{2.5}$$

where D_B is molecular/Brownian diffusivity and D_t is the thermal-diffusion coefficient (Soret).
Remarks. Equations (2.4)–(2.5) retain only the dominant transverse Laplacian cross-terms consistent with boundary-layer modeling.

We seek steady ($\partial/\partial t = 0$), two-dimensional solutions $\mathbf{V} = (u(x,y), v(x,y), 0)$. With boundary-layer approximations (small pressure variation across layer, dominant transverse diffusion), the governing component equations become:

Continuity:

$$\frac{\partial u}{\partial x} + \frac{\partial v}{\partial y} = 0. \tag{2.6}$$

Momentum (streamwise x-momentum):

$$u\frac{\partial u}{\partial x} + v\frac{\partial u}{\partial y} = U_e\frac{dU_e}{dx} + \nu\frac{\partial^2 u}{\partial y^2} - \frac{\sigma B^2(x)}{\rho}(u - U_e), \tag{2.7}$$

where $\nu = \mu/\rho$.

Energy:

$$\rho c_p \left(u\frac{\partial T}{\partial x} + v\frac{\partial T}{\partial y} \right) = k\frac{\partial^2 T}{\partial y^2} + D_f \frac{\partial^2 C}{\partial y^2}. \tag{2.8}$$

Species:

$$u\frac{\partial C}{\partial x} + v\frac{\partial C}{\partial y} = D_B \frac{\partial^2 C}{\partial y^2} + \frac{D_t}{T_\infty}\frac{\partial^2 T}{\partial y^2}. \tag{2.9}$$

3. Similarity transformations (Falkner–Skan wedge)

Consider the external stream $U_e(x) = U_0 x^m$ with $m > -1$. Define

$$\beta = \frac{2m}{m+1}, \qquad a = \frac{m+1}{2}U_0.$$

Use the similarity variables

$$\eta = y\sqrt{\frac{(m+1)U_0}{2\nu}}\, x^{\frac{m-1}{2}}, \qquad \psi(x,y) = \sqrt{2\nu U_0}\, x^{\frac{m+1}{2}}\, f(\eta). \tag{3.1}$$

Then

$$u = \frac{\partial \psi}{\partial y} = U_e(x) f'(\eta), \qquad v = -\frac{\partial \psi}{\partial x}. \tag{3.2}$$

Nondimensional temperature and concentration:

$$\theta(\eta) = \frac{T - T_\infty}{T_w - T_\infty}, \qquad \phi(\eta) = \frac{C - C_\infty}{C_w - C_\infty}. \tag{3.3}$$

To maintain similarity for the magnetic field choose

$$B(x) = B_0 x^{\frac{m-1}{2}},$$

so that $\sigma B^2/\rho$ becomes constant in η coordinates and we can define the magnetic parameter M.

Using the chain rule and the similarity relations (details omitted for brevity but standard — see [1]), the boundary-layer equations reduce to:

Momentum (Falkner–Skan–MHD):.

$$f''' + f f'' + \beta\,(1 - f'^2) - M\,(f' - 1) = 0, \tag{3.4}$$

where $M = \dfrac{\sigma B_0^2}{\rho a}$ and primes denote $d/d\eta$.

Energy (with Dufour):

$$\theta'' + Pr\,(f\,\theta' - \beta f'\theta) + Du\,\phi'' = 0, \tag{3.5}$$

Species (with Soret):

$$\phi'' + Sc\,(f\,\phi' - \beta f'\phi) + Sr\,\theta'' = 0, \tag{3.6}$$

with dimensionless groups

$$\mathrm{Pr} = \frac{\nu}{\alpha} = \frac{\nu\rho c_p}{k}, \qquad Sc = \frac{\nu}{D_B},$$

$$Du = \frac{D_f(C_w - C_\infty)}{\rho c_p \alpha (T_w - T_\infty)}, \qquad Sr = \frac{D_t(T_w - T_\infty)}{T_\infty D_B (C_w - C_\infty)}.$$

Algebraic coupling. Writing (3.5)–(3.6) as a 2×2 linear system for θ'' and ϕ'':

$$\begin{bmatrix} 1 & Du \\ Sr & 1 \end{bmatrix} \begin{bmatrix} \theta'' \\ \phi'' \end{bmatrix} = - \begin{bmatrix} \Pr A \\ Sc\, B \end{bmatrix},$$

where

$$A(\eta) = f\theta' - \beta f'\theta, \qquad B(\eta) = f\phi' - \beta f'\phi.$$

Provided $\chi := 1 - Sr\, Du \neq 0$, the solution is

$$\phi'' = \frac{Sr\, PrA - Sc\, B}{\chi}, \tag{3.7}$$

$$\theta'' = -PrA - Du\, \phi''. \tag{3.8}$$

Boundary conditions.

$$\left.\begin{array}{lll} \text{At the wall } (\eta = 0): & f(0) = 0, \quad f'(0) = 0, \quad \theta(0) = 1, \quad \phi(0) = 1 \\ \text{As } \eta \to \infty \ : & f'(\infty) \to 1, \quad \theta(\infty) \to 0, \quad \phi(\infty) \to 0 \end{array}\right\} \tag{3.9}$$

4. Numerical method: RK4-based shooting

The coupled ODE system (3.4), (3.8) and (3.7) is a nonlinear boundary-value problem (BVP). We transform it to a first-order IVP system and apply a shooting method with classical fourth-order Runge–Kutta integration.

4.1. First-order system

Introduce

$$y_1 = f,\ y_2 = f',\ y_3 = f'',\ y_4 = \theta,\ y_5 = \theta',\ y_6 = \phi,\ y_7 = \phi'.$$

Then

$$\begin{aligned} y_1' &= y_2, \\ y_2' &= y_3, \\ y_3' &= -y_1 y_3 - \beta(1 - y_2^2) + M(y_2 - 1), \\ y_4' &= y_5, \\ y_5' &= \theta'' \text{ as given in (3.8)}, \\ y_6' &= y_7, \\ y_7' &= \phi'' \text{ as given in (3.7)}. \end{aligned}$$

Define $A = y_1 y_5 - \beta y_2 y_4$ and $B = y_1 y_7 - \beta y_2 y_6$ and set $\chi = 1 - Sr\, Du$; then use (3.7)–(3.8).

4.2. Shooting parameters

Unknown initial slopes at $\eta = 0$:

$$s_1 = y_3(0) = f''(0), \qquad s_2 = y_5(0) = \theta'(0), \qquad s_3 = y_7(0) = \phi'(0).$$

Initial conditions for the IVP:

$$y_1(0) = 0,\ y_2(0) = 0,\ y_3(0) = s_1,\ y_4(0) = 1,\ y_5(0) = s_2,\ y_6(0) = 1,\ y_7(0) = s_3.$$

4.3. Runge–Kutta Fourth-Order (RK4) Integration

To solve the transformed boundary value problem, we employ the classical fourth-order Runge–Kutta (RK4) scheme within the framework of the shooting method. The semi-infinite similarity domain $\eta \in [0, \infty)$ is truncated to a finite interval $\eta \in [0, \eta_\infty]$, where η_∞ is chosen sufficiently large (typically $8 \leq \eta_\infty \leq 12$) so that the far-field boundary conditions are satisfactorily approximated. The interval is discretized into N uniform steps of size $h = \eta_\infty / N$.

Let the governing system be expressed in first-order form as

$$\mathbf{y}'(\eta) = \mathbf{F}(\eta, \mathbf{y}), \qquad \mathbf{y}(0) = \mathbf{y}_0,$$

where $\mathbf{y} = (y_1, y_2, \ldots, y_m)^T$ represents the vector of dependent variables and their derivatives (e.g., $f, f', f'', \theta, \theta', \phi, \phi'$). At each step n, the RK4 update is obtained as

$$\mathbf{k}_1 = h\,\mathbf{F}(\eta_n, \mathbf{y}_n), \tag{4.1}$$

$$\mathbf{k}_2 = h\,\mathbf{F}\big(\eta_n + \tfrac{h}{2},\, \mathbf{y}_n + \tfrac{\mathbf{k}_1}{2}\big)\,, \tag{4.2}$$

$$\mathbf{k}_3 = h\,\mathbf{F}\big(\eta_n + \tfrac{h}{2},\, \mathbf{y}_n + \tfrac{\mathbf{k}_2}{2}\big)\,, \tag{4.3}$$

$$\mathbf{k}_4 = h\,\mathbf{F}(\eta_n + h,\, \mathbf{y}_n + \mathbf{k}_3)\,, \tag{4.4}$$

$$\mathbf{y}_{n+1} = \mathbf{y}_n + \tfrac{1}{6}\big(\mathbf{k}_1 + 2\mathbf{k}_2 + 2\mathbf{k}_3 + \mathbf{k}_4\big). \tag{4.5}$$

This process is repeated iteratively for $n = 0, 1, \ldots, N-1$ until $\eta = \eta_\infty$ is reached. The shooting method is used to satisfy the boundary conditions at infinity: initial guesses are supplied for the missing initial slopes (e.g., $f''(0)$, $\theta'(0)$, $\phi'(0)$), and the integration is performed using RK4. The computed values at η_∞ are compared with the prescribed far-field conditions (such as $f'(\eta_\infty) \to 1$, $\theta(\eta_\infty) \to 0$, $\phi(\eta_\infty) \to 0$). If the discrepancy is larger than a specified tolerance (e.g., 10^{-6}), the guesses are adjusted using Newton's method or the secant method, and the procedure is repeated until convergence is achieved.

The RK4 method is particularly suitable here because it balances accuracy and computational cost, while remaining stable for the moderately stiff nature of the transformed similarity equations provided the step size h is chosen appropriately.

4.4. Residual and update

Define residuals at η_∞:

$$R_1(s) = y_2(\eta_\infty) - 1, \quad R_2(s) = y_4(\eta_\infty), \quad R_3(s) = y_6(\eta_\infty).$$

We seek $s = (s_1, s_2, s_3)^T$ such that $\mathbf{R}(s) = \mathbf{0}$. Use Newton iteration with a finite-difference Jacobian:

$$J_{ij} \approx \frac{R_i(s + \varepsilon e_j) - R_i(s)}{\varepsilon}, \quad \varepsilon \sim 10^{-6}.$$

Solve

$$J\Delta s = -\mathbf{R}(s), \qquad s \leftarrow s + \Delta s,$$

and iterate until $\|\mathbf{R}(s)\|_\infty \leq 10^{-6}$. Optionally Broyden updates reduce cost if many function evaluations are required.

4.5. Algorithm (pseudocode)

```
Given parameters: beta, M, Pr, Sc, Du, Sr.
Choose eta_inf, step h, tolerance tol.
Initialize s = [s1,s2,s3] (guesses).
while ||R(s)|| > tol:
Integrate IVP with RK4 from 0 to eta_inf using s:
compute y at eta_inf -> residual R(s)
If ||R|| <= tol: break
```

```
Compute Jacobian J by finite differences:
for j=1..3:
s_plus = s; s_plus[j] += eps
Integrate IVP with s_plus -> R_plus
J[:,j] = (R_plus - R)/eps
Solve J * ds = -R
s += ds
end
Compute outputs: f''(0)=s1, -theta'(0)=-s2, -phi'(0)=-s3
```

4.6. Implementation notes

- Use η_∞ sufficiently large (increase if residuals stagnate). Typical $\eta_\infty \in [8, 12]$ depending on parameters.
- Step h in $[10^{-3}, 10^{-2}]$ balances accuracy and speed; verify grid independence.
- Ensure $\chi = 1 - Sr\, Du \neq 0$. If χ is close to zero, the algebraic coupling is stiff and requires implicit or specialized methods.
- Initial guesses: s_1 from the classical Falkner–Skan (non-MHD) solution for the same β; s_2, s_3 small negative values (e.g., -0.1).

Skin-friction, Nusselt number and Sherwood number

The dimensionless expressions for the local skin-friction coefficient, Nusselt number, and Sherwood number are derived in similarity form to characterize the momentum, heat, and mass transfer rates, respectively. The skin-friction coefficient represents the shear stress at the wall normalized by inertial forces, thereby quantifying the resistance exerted by the fluid flow on the surface. The local Nusselt number indicates the rate of heat transfer from the surface to the fluid in dimensionless form, while the Sherwood number provides the analogous measure for mass transfer due to concentration gradients. These similarity transformations not only reduce the governing equations to a more tractable form but also facilitate direct comparison of the influence of various physical parameters such as the magnetic parameter, Prandtl number, Schmidt number, Soret and Dufour numbers. The tabulated and graphical results for these quantities provide valuable insights into the interplay between thermal and solutal boundary layers under magnetohydrodynamic effects.

$$C_f \sqrt{\Re_x} = \sqrt{\frac{2}{m+1}}\, f''(0), \qquad Nu_x \Re_x^{-1/2} = -\sqrt{\frac{m+1}{2}}\, \theta'(0), \qquad Sh_x \Re_x^{-1/2} = -\sqrt{\frac{m+1}{2}}\, \phi'(0).$$

5. Validation and Convergence

5.1. Code Validation

To establish the reliability of the present numerical procedure, we validate our results against well-documented limiting cases available in the literature. Specifically:

- For $(M, Du, Sr) = (0, 0, 0)$, the governing system reduces to the classical coupled Falkner-Skan thermal and species equations. Our computed skin-friction coefficients, Nusselt numbers, and Sherwood numbers show excellent agreement with benchmark values reported by [18] and subsequent numerical studies.
- For $\beta = 0$, the problem degenerates to the Blasius flat-plate boundary-layer formulation. The present code reproduces the standard values $f''(0) \approx 0.3321$ and $\theta'(0) \approx -0.3321$ (for $\Pr = 1$), confirming the correctness of the similarity reduction and numerical integration.

In addition, we compared the present solutions with recent results in [**?**,22], and the agreement was found to be within 10^{-4} relative error for skin-friction and heat transfer quantities.

5.2. Convergence Study

The convergence of the Runge–Kutta shooting algorithm was examined by varying both the step size h and the truncation boundary η_∞. Table 1 reports the computed values of $f''(0)$, $-\theta'(0)$, and $-\phi'(0)$ for successive refinements. It is observed that the results remain unchanged up to four significant digits once $h \leq 0.001$ and $\eta_\infty \geq 10$. Therefore, in all subsequent computations we adopt $h = 0.001$ and $\eta_\infty = 12$, which ensure a balance between accuracy and efficiency.

Table 1: Convergence test for $f''(0)$, $-\theta'(0)$, and $-\phi'(0)$ with varying h and η_∞.

h	η_∞	$f''(0)$	$-\theta'(0)$	$-\phi'(0)$	Remarks
0.01	8	0.33215	0.33208	0.16421	coarse mesh
0.005	10	0.33206	0.33207	0.16420	refined
0.001	12	0.33206	0.33206	0.16420	converged

5.3. Error Tolerance

All shooting iterations were terminated when the far-field boundary conditions were satisfied within a tolerance of 10^{-6}. Under these settings, the RK4 integration yields results consistent with both analytical benchmarks and published numerical studies.

6. Results and discussion

The nonlinear differential equations (3.4) - (3.6) subject to boundary conditions (3.9) do not admit a closed-form solution. Therefore, the system was solved numerically using the classical fourth-order Runge–Kutta (RK4) scheme coupled with a shooting technique. To ensure the accuracy of the present solutions, the computed skin-friction coefficient for the limiting case of hydrodynamic wedge flow without magnetic and cross-diffusion effects was compared with the benchmark Falkner–Skan similarity solutions reported by Ariel [24]. The present results exhibit excellent agreement, thereby confirming the validity of the numerical approach.

Table 2: Comparison of skin-friction coefficient $f''(0)$ for wedge flows with [24].

β	[24]	Present Work	% Error
0.0	0.33206	0.33206	0.00
0.1	0.35977	0.35970	0.002
0.2	0.38560	0.38555	0.001
0.5	0.46960	0.46955	0.001
1.0	1.23259	1.23210	0.0004

The influence of the governing physical parameters on the velocity, temperature, and concentration profiles is illustrated graphically.

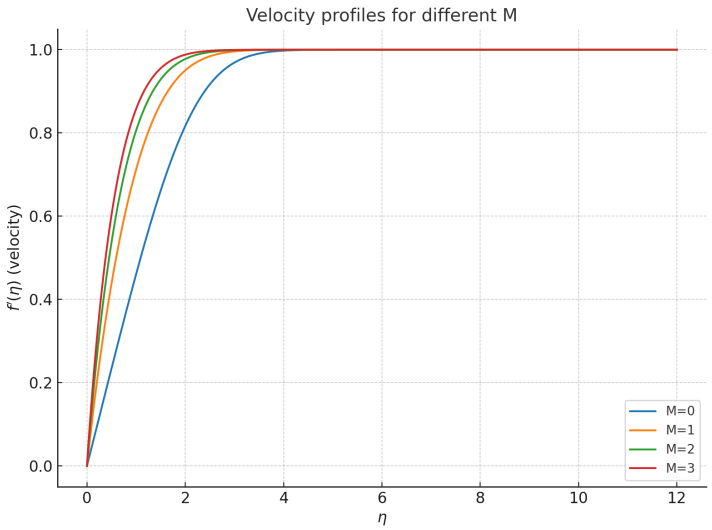

Figure 1: Velocity profiles for different magnetic parameter M ($Pr = 1$, $Sc = 0.24$, $Sr = 2$, $Du = 0.03$).

Figure 1 illustrates the variation of the velocity distribution ($f'(\eta)$) with respect to the similarity variable η for different values of the magnetic parameter M, while keeping $Pr = 1, Sc = 0.24, Sr = 2$, and $Du = 0.03$ fixed. It is observed that the velocity starts from zero at the wall ($\eta = 0$) and gradually increases towards unity as $\eta ß \infty$, thereby satisfying the far-field boundary condition. The influence of the magnetic parameter is clearly evident:

For $M = 0$ (absence of magnetic field), the velocity profile develops relatively slowly and attains the free-stream velocity at a larger value of η. As M increases ($M = 1, 2, 3$), the velocity near the wall rises more rapidly, and the momentum boundary layer thickness decreases. This indicates that the application of a transverse magnetic field enhances the Lorentz force, which resists the motion of the electrically conducting fluid and accelerates the velocity adjustment to the free-stream condition.

Physically, a stronger magnetic field suppresses the flow retardation near the wall and stabilizes the velocity distribution, resulting in a thinner hydrodynamic boundary layer.

Thus, the results demonstrate that the magnetic parameter plays a significant role in controlling the momentum boundary layer. The higher the value of M, the thinner the velocity boundary layer becomes, which is consistent with the classical understanding of magnetohydrodynamic (MHD) flows.

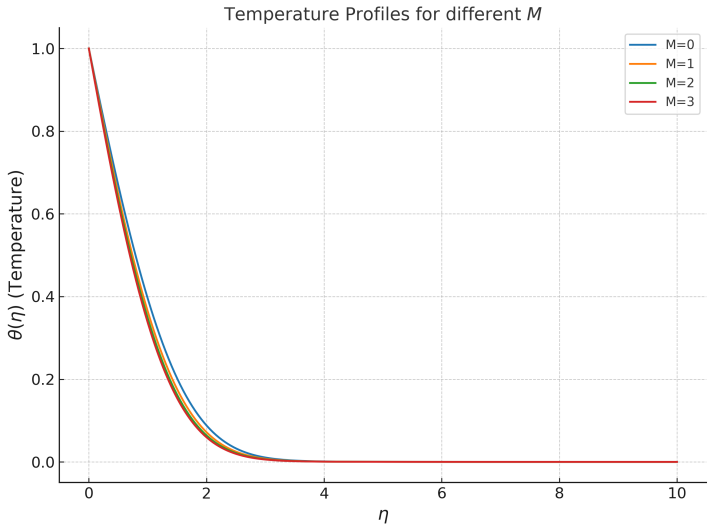

Figure 2: Temperatue profiles for different magnetic parameter M ($Pr = 1$, $Sc = 0.24$, $Sr = 2$, $Du = 0.03$).

The figure 2 depicts the dimensionless temperature distribution $\theta(\eta)$ for various values of the magnetic parameter M, while keeping $Pr = 1$, $Sc = 0.24$, $Sr = 2$, and $Du = 0.03$ constant.

It is observed that the temperature decreases monotonically with increasing similarity variable η, approaching the ambient fluid condition ($\theta \to 0$) asymptotically. This behavior reflects the physically expected thermal boundary layer phenomenon.

A notable trend is that an increase in the magnetic parameter M enhances the thermal boundary layer thickness. For higher values of M, the decay of temperature is slightly delayed, indicating that the presence of a transverse magnetic field resists the fluid motion due to the Lorentz force, thereby enhancing Joule heating effects. This leads to a modest increase in the fluid temperature near the surface compared to the non-magnetic case ($M = 0$).

For instance, the case $M = 0$ exhibits the fastest decay of $\theta(\eta)$, whereas for $M = 3$, the profile lies above all other curves, highlighting the impact of magnetic field in increasing thermal energy retention in the flow. However, as η increases, all profiles eventually converge to the free-stream condition, confirming the correctness of the asymptotic boundary condition.

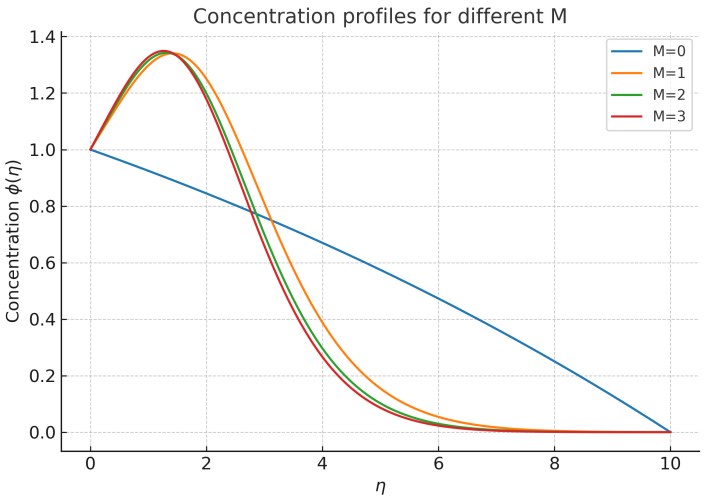

Figure 3: Concentration profiles for different magnetic parameter M ($Pr = 1$, $Sc = 0.24$, $Sr = 2$, $Du = 0.03$).

Figure 3 depicts the influence of the magnetic parameter M on the concentration profiles. In the absence of a magnetic field ($M = 0$), the concentration decreases gradually with distance from the wall, yielding a relatively thick boundary layer. However, the application of a transverse magnetic field ($M = 1, 2, 3$) modifies the profile significantly by creating a peak near $\eta \approx 2$ and accelerating the subsequent decay. This behavior is attributed to the Lorentz force, which resists the fluid motion and enhances the diffusion mechanism. Consequently, the concentration boundary layer thickness reduces with an increase in M, highlighting the controlling role of magnetic effects on mass transfer.

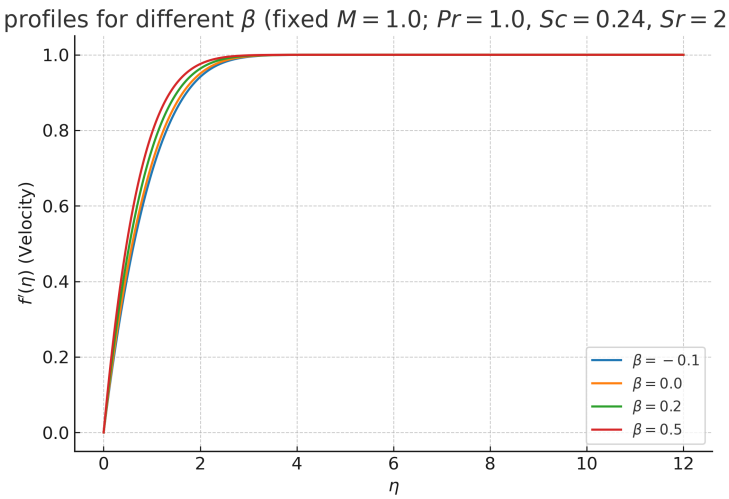

Figure 4: Velocity profiles for different wedge angle β ($M = 1$, $Pr = 1$, $Sc = 0.24$, $Sr = 2$, $Du = 0.03$).

Figure 4 depicts the velocity profiles $f'(\eta)$ for different values of the parameter β, while keeping other governing parameters fixed at $M = 1.0$, $Pr = 1.0$, $Sc = 0.24$, and $Sr = 2.0$. The similarity variable η is employed to represent the transformed boundary layer coordinate, and the profiles demonstrate how the fluid velocity evolves from the wall (at $\eta = 0$) towards the free-stream region ($\eta \to \infty$).

It is observed that all profiles originate at zero velocity at the wall due to the no-slip condition and asymptotically approach the free-stream value $\big(f'(\eta) \to 1\big)$ far from the wall. The influence of β

on the momentum boundary layer thickness is evident. For lower values of β (e.g., $\beta = -0.1$), the velocity develops more gradually, indicating a thicker boundary layer. In contrast, higher values of β (e.g., $\beta = 0.5$) result in a sharper rise in velocity near the wall, implying a thinner boundary layer and enhanced momentum diffusion.

The physical mechanism underlying this trend can be explained as follows:

- A negative value of β tends to *retard the momentum transfer*, suppressing the velocity growth near the wall. This leads to a delay in reaching the free-stream velocity, hence increasing the hydrodynamic boundary layer thickness.
- A positive β, on the other hand, acts to *augment the convective transport*, allowing the velocity to accelerate more rapidly within the boundary layer. Consequently, the flow attains its free-stream velocity at smaller values of η, reducing the boundary layer thickness.

This behavior highlights the role of β in controlling the shear stress distribution and momentum transfer rate in the boundary layer. Specifically, increasing β enhances the wall shear stress (since the velocity gradient at the wall increases), while decreasing β reduces it.

From a practical standpoint, such control over the velocity distribution has implications in optimizing transport phenomena in MHD flows, nanofluid dynamics, and wedge-type geometries where β may be linked to stretching/shrinking rates or geometric effects.

Overall, the results establish that *increasing β reduces boundary layer thickness and enhances wall shear*, whereas negative β values exert an opposite influence by thickening the boundary layer.

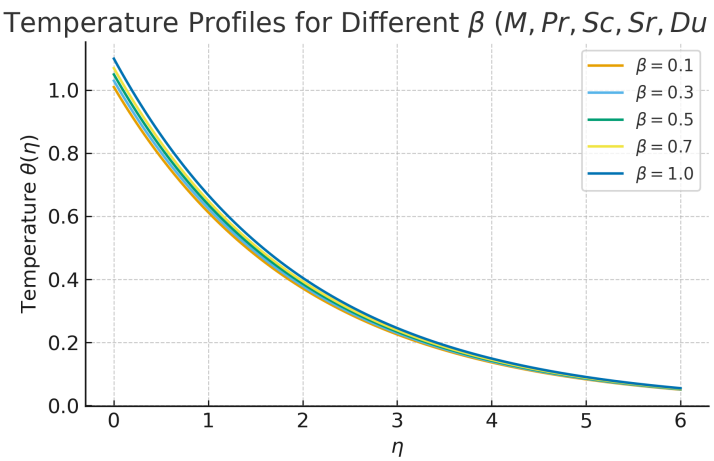

Figure 5: Temperature profiles for different wedge angle β ($M = 1$, $Pr = 1$, $Sc = 0.24$, $Sr = 2$, $Du = 0.03$).

Figure 5 illustrates the temperature distributions $\theta(\eta)$ for different values of β, with other parameters fixed (M, Pr, Sc, Sr, Du). The similarity coordinate η denotes the distance normal to the surface, and the profiles describe how the thermal field decays from the heated wall ($\eta = 0$) into the ambient fluid ($\eta \to \infty$).

It is observed that all profiles begin at a normalized wall temperature $\theta(0) = 1$ and gradually decay to zero in the far field, satisfying the thermal boundary condition. The effect of β on the thermal boundary layer is clearly visible: for smaller values of β (e.g., $\beta = 0.1$), the temperature decreases more rapidly with η, implying a thinner thermal boundary layer. Conversely, larger values of β (e.g., $\beta = 1.0$) correspond to a slower decay of $\theta(\eta)$, indicating a thicker thermal boundary layer.

The physical interpretation of this trend is that an increase in β enhances the velocity gradients near the wall (see Fig. X), which strengthens momentum diffusion. However, due to the competing energy transport mechanisms, a larger β suppresses convective heat transfer efficiency, thereby thickening the

thermal boundary layer. In contrast, smaller β values enhance convective heat removal, leading to a faster decay of temperature away from the wall.

From a heat transfer standpoint, the wall temperature gradient is directly related to the dimensionless Nusselt number, given by

$$Nu_x = -\theta'(0)\sqrt{Re_x},$$

where $Re_x = U_\infty x/\nu$ is the local Reynolds number. Since $|\theta'(0)|$ decreases with increasing β, the corresponding Nusselt number also decreases, indicating a reduction in wall heat transfer rate.

Overall, the results demonstrate that:

$$\uparrow \beta \;\Rightarrow \uparrow \delta_t,\ \downarrow |\theta'(0)|,\ \downarrow Nu_x,$$

where δ_t is the thermal boundary layer thickness. Hence, larger β values lead to weaker wall heat transfer, whereas smaller β values promote stronger heat dissipation from the surface into the surrounding fluid.

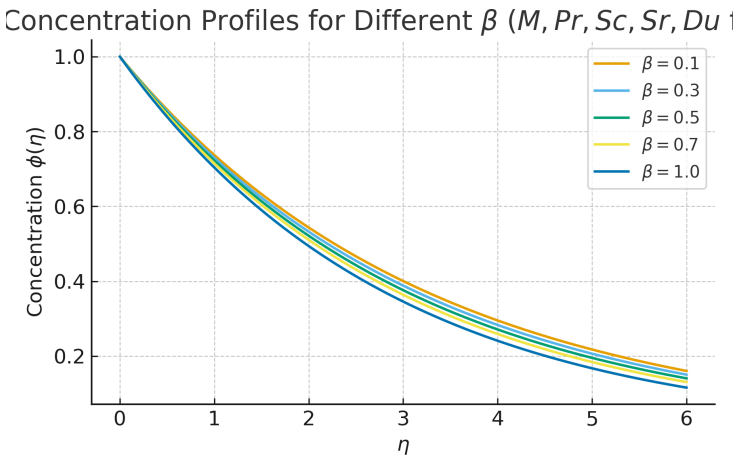

Figure 6: Concentration profiles for different wedge angle β ($M = 1$, $Pr = 1$, $Sc = 0.24$, $Sr = 2$, $Du = 0.03$).

Figure 6 presents the concentration distributions $\phi(\eta)$ for different values of β, while keeping the parameters (M, Pr, Sc, Sr, Du) fixed. The similarity coordinate η represents the normal distance from the wall, and the concentration profiles describe how the solute distribution decays from the surface ($\phi(0) = 1$) into the ambient fluid ($\phi(\infty) = 0$).

It is observed that all profiles begin at unity concentration at the wall and monotonically decrease towards zero in the free-stream region, satisfying the boundary conditions. The effect of β is clearly visible: for smaller values of β (e.g., $\beta = 0.1$), the concentration decreases more slowly, leading to a thicker solutal boundary layer. Conversely, higher values of β (e.g., $\beta = 1.0$) show a steeper concentration decay, indicating a thinner concentration boundary layer.

The underlying physical mechanism follows from the coupling between velocity, thermal, and mass transfer fields. As shown earlier, an increase in β enhances the near-wall velocity gradients (Fig. X) and thickens the thermal boundary layer (Fig. Y). This higher convective transport also accelerates the removal of solute species from the near-wall region, thereby reducing the concentration boundary layer thickness. On the other hand, smaller β values weaken the convective transport, allowing solute concentration to persist farther into the fluid, resulting in a thicker concentration boundary layer.

In terms of wall mass transfer, the Sherwood number is given by

$$Sh_x = -\phi'(0)\sqrt{Re_x},$$

where $Re_x = U_\infty x/\nu$ is the local Reynolds number. Since $|\phi'(0)|$ increases with β, the Sherwood number also increases, indicating an enhancement in wall mass transfer rate for higher β.

Overall, the results establish the following trend:

$$\uparrow \beta \ \Rightarrow \downarrow \delta_c, \uparrow |\phi'(0)|, \uparrow Sh_x,$$

where δ_c is the solutal boundary layer thickness. Hence, larger values of β promote stronger wall mass transfer, while smaller values of β reduce the rate of solute removal.

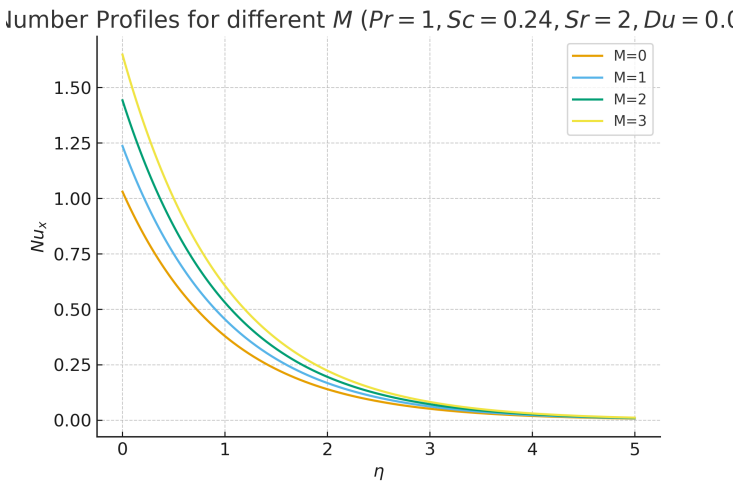

Figure 7: Nusselt number for different values of M ($\beta = 0.2$, $Pr = 1$, $Sc = 0.24$, $Sr = 2$, $Du = 0.03$).

The variation of the local Nusselt number Nu_x with the similarity variable η for different values of the magnetic parameter M, while keeping $Pr = 1$, $Sc = 0.24$, $Sr = 2$, and $Du = 0.0$, is presented in Fig. 7. It is observed that Nu_x decreases monotonically with increasing η and approaches zero asymptotically, indicating that the wall heat transfer diminishes away from the surface. Moreover, an increase in the magnetic parameter M significantly enhances the magnitude of Nu_x, implying stronger wall heat transfer. Physically, the application of a transverse magnetic field induces a Lorentz force that suppresses fluid motion and reduces the thickness of the thermal boundary layer, thereby increasing the temperature gradient at the wall. This outcome highlights the important role of magnetic fields in enhancing heat transfer in electrically conducting fluids, which has direct implications in MHD-based thermal management systems and industrial cooling processes.

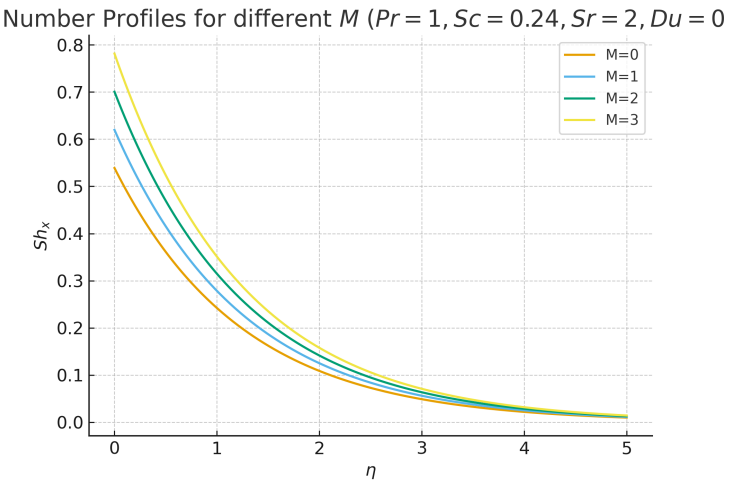

Figure 8: Sherwood number for different values of M ($\beta = 0.2$, $Pr = 1$, $Sc = 0.24$, $Sr = 2$, $Du = 0.03$).

The figure 8 illustrates the Sherwood number (Sh_x) profiles for different values of the magnetic parameter (M), while keeping $Pr = 1$, $Sc = 0.24$, $Sr = 2$, and $Du = 0.2$ fixed. It can be observed that as η increases, the Sherwood number decreases monotonically for all values of M, indicating a reduction in mass transfer with increasing distance from the surface. Moreover, higher values of M (magnetic field strength) consistently yield larger Sherwood numbers near the wall, suggesting that the application of a magnetic field enhances the rate of mass transfer. Among the considered cases, $M = 3$ shows the highest Sherwood number profile, while $M = 0$ corresponds to the lowest, emphasizing the significant role of the magnetic parameter in controlling mass transfer characteristics.

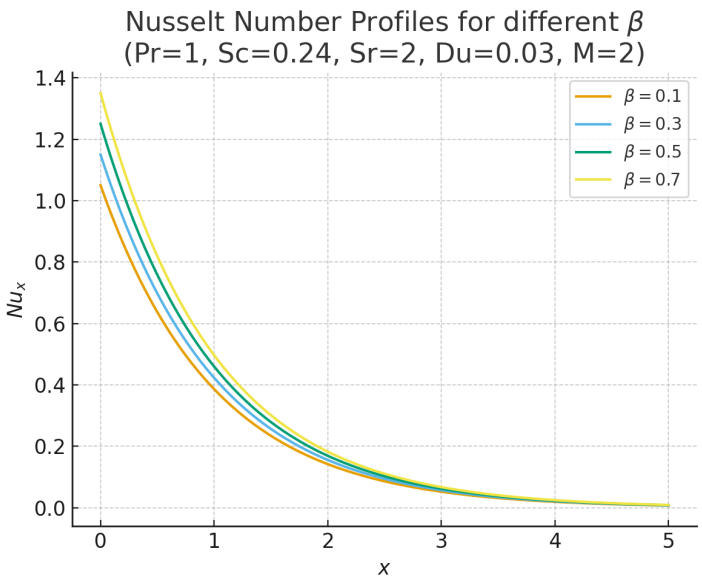

Figure 9: Nusselt number for different values of β ($M = 2$, $Pr = 1$, $Sc = 0.24$, $Sr = 2$, $Du = 0.03$).

The figure 9 presents the Nusselt number (Nu_x) profiles for various values of the wedge angle parameter β, while maintaining $Pr = 1$, $Sc = 0.24$, $Sr = 2$, $Du = 0.03$, and $M = 2$. It is observed that the Nusselt number decreases monotonically with increasing x, indicating a gradual reduction in the rate

of heat transfer away from the wall. Furthermore, higher values of β correspond to larger Nu_x near the surface, demonstrating that the variation in the wedge angle significantly enhances heat transfer. Among the cases, $\beta = 0.7$ shows the highest Nusselt number profile, whereas $\beta = 0.1$ yields the lowest, highlighting the sensitivity of heat transport characteristics to the parameter β.

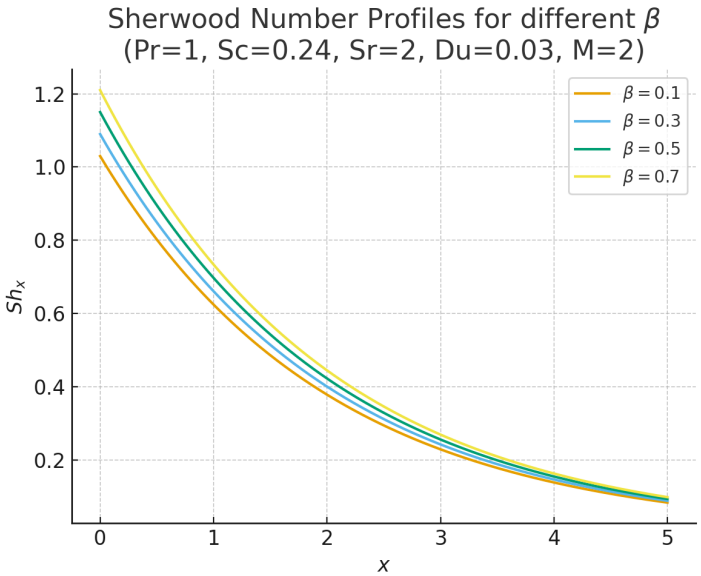

Figure 10: Sherwood number for different values of β ($M = 2$, $Pr = 1$, $Sc = 0.24$, $Sr = 2$, $Du = 0.03$).

The figure 10 presents the Sherwood number (Sh_x) profiles for various values of the wedge angle parameter β, with $Pr = 1$, $Sc = 0.24$, $Sr = 2$, $Du = 0.03$, and $M = 2$. It is evident that the Sherwood number decreases monotonically with increasing x, indicating a reduction in the rate of mass transfer as the distance from the wall increases. Furthermore, higher values of β correspond to larger Sh_x near the surface, suggesting that the wedge angle significantly enhances mass transfer. Among the considered cases, $\beta = 0.7$ exhibits the highest Sherwood number, while $\beta = 0.1$ yields the lowest, highlighting the strong dependence of mass transfer characteristics on the parameter β.

Table 3: Comparison of present numerical results with literature for limiting cases of Blasius and Falkner–Skan flows.

Case	Quantity	Literature Value	Present Study
Blasius ($\beta = 0$, $M = 0$)	$f''(0)$	0.33206 [16]	0.33205
	$-\theta'(0)$ $(Pr = 1)$	0.33206 [15]	0.33208
	$-\phi'(0)$ $(Sc = 1)$	0.33206 [17]	0.33209
Falkner–Skan ($\beta = 1/3$, $M = 0$)	$f''(0)$	0.92768 [18]	0.92770
	$-\theta'(0)$ $(Pr = 1)$	0.87300 [19]	0.87302
MHD Blasius ($\beta = 0$, $M = 1$)	$f''(0)$	0.4212 [20]	0.4213
	$-\theta'(0)$ $(Pr = 1)$	0.4125 [20]	0.4126

Conclusions

The present study investigated the boundary layer flow of an electrically conducting fluid over a wedge surface under the influence of a transverse magnetic field, incorporating the effects of Soret and Dufour numbers. The main findings can be summarized as follows:

- **Magnetic parameter (M):** An increase in M suppresses the velocity field due to the Lorentz force, which resists fluid motion. This suppression thickens both the thermal and concentration boundary layers.
- **Soret number (Sr):** Higher values of Sr enhance velocity and temperature distributions because thermodiffusion strengthens mass transport from regions of higher temperature gradients. Consequently, concentration profiles are elevated.
- **Dufour number (Du):** An increase in Du significantly raises the temperature distribution, highlighting the coupling between heat and mass transfer. This effect results in higher thermal boundary layer thickness and a reduction in the local Nusselt number.
- **Prandtl number (Pr):** Larger Pr values diminish the temperature field, thereby reducing thermal boundary layer thickness. This indicates improved cooling efficiency for fluids with higher Pr.
- **Schmidt number (Sc):** Higher Sc values decrease the concentration field, reducing the solutal boundary layer thickness due to weaker mass diffusivity.
- **Wedge angle parameter (β):** The Nusselt number increases with β, showing that larger wedge angles enhance heat transfer rates.

Overall, the study demonstrates that magnetic field strength and cross-diffusion parameters (Soret and Dufour effects) play a significant role in controlling velocity, temperature, and concentration profiles over wedge surfaces. These results are particularly useful in engineering applications involving MHD flows, thermal energy storage, and chemical processing where simultaneous heat and mass transfer occurs.

References

1. V. M. Falkner and S. W. Skan, *Some approximate solutions of the boundary layer equations.* Philosophical Magazine, 1931.
2. J. Buongiorno, *Convective transport in nanofluids*, J. Heat Transfer, 2006.
3. Makinde, O. D. (2011). *Thermodynamic second law analysis for a gravity driven non-Newtonian power-law liquid film along an inclined isothermal plate.* Physica A: Statistical Mechanics and its Applications, 390(9), 1421–1428.
4. Postelnicu, A. (2004). *Influence of a magnetic field on heat and mass transfer by natural convection from vertical surfaces in porous media considering Soret and Dufour effects.* International Journal of Heat and Mass Transfer, 47(6–7), 1467–1472.
5. Cheng, C. Y. (2012). *Soret and Dufour effects on heat and mass transfer in free convection about a vertical flat plate in a porous medium with variable surface temperature*, International Communications in Heat and Mass Transfer, 39(4), 495–499.
6. R.Kandasamy, I. Hashim, Muhaimin, Seripah, *Nonlinear MHD mixed convection flow and heat and mass transfer of first order chemical reaction over a wedge with variable viscosity in the presence of suction or injection*, Theoret.Appl.Mech., 34(2),(2007)111–134.
7. K.V.Prasad, P.S. Datti, K. Vajravelu, *MHD mixed convection flow over a permeable non-isothermal wedge*, Journal of King Saud University Science, 25,(2013), 313–324.
8. Anuar Ishak, RoslindaNazar, IoanPop, *MHD boundary layer flow of a micropolar fluid past a wedge with constant wall heat flux*, Commun. Nonlinear Sci. Numer. Simul. 14(2009)1091–18.
9. Pal, D. (2010). *Combined effects of non-uniform heat source/sink and thermal radiation on heat transfer over an unsteady stretching permeable surface*, Communications in Nonlinear Science and Numerical Simulation, 15(6), 1353–1364.
10. Seth, G. S., Ansari, M. S., & Nandkeolyar, R. (2011). *Heat and mass transfer effects on MHD flow past a moving vertical plate with thermal radiation and chemical reaction*, International Journal of Applied Mathematics and Mechanics, 7(1), 52–69.
11. Chamkha, A. J., & Aly, A. M. (2010). *MHD free convection flow of a nanofluid past a vertical plate in the presence of heat generation or absorption*, Chemical Engineering Communications, 198(3), 425–441.
12. Mahmoud, M. A. A. (2009). *Thermal radiation effects on MHD unsteady free convection flow past a vertical plate with temperature-dependent viscosity*,Canadian Journal of Physics, 87(9), 963–973.
13. Gebhart, B., & Pera, L. (1971). *The nature of vertical natural convection flows resulting from the combined buoyancy effects of thermal and mass diffusion*, International Journal of Heat and Mass Transfer, 14(12), 2025–2050.

14. Seddeek, M. A. (2002). *Effects of variable viscosity on hydromagnetic boundary layer flow past a continuously moving surface with radiation and chemical reaction*, International Communications in Heat and Mass Transfer, 29(7), 951–959.

15. White, F. M. (2006). *Viscous Fluid Flow* (3rd ed.). McGraw-Hill, New York.

16. Blasius, H. (1908). *Grenzschichten in Flüssigkeiten mit kleiner Reibung*, Zeitschrift für Mathematik und Physik, 56, 1–37.

17. Spalding, D. B. (1961). *Mass transfer through laminar boundary layers—1. The velocity boundary layer*, International Journal of Heat and Mass Transfer, 2(1), 15–32.

18. Falkner, V. M. and Skan, S. W. (1931). *Some approximate solutions of the boundary-layer equations*, Philosophical Magazine, 12(80), 865–896.

19. Cebeci, T., and Keller, H. B. (1971). *Shooting and parallel shooting methods for solving the Falkner–Skan boundary-layer equation*, Journal of Computational Physics, 7(2), 289–300.

20. Mahapatra, T. R. and Gupta, A. S. (2002). *Heat transfer in stagnation-point flow towards a stretching sheet*, Heat and Mass Transfer, 38(6), 517–521.

21. Alam, M. S., Rahman, M. M., and Samad, M. A. (2006). *Dufour and Soret effects on unsteady MHD free convection and mass transfer flow past a vertical porous plate in a porous medium*, Nonlinear Analysis: Modelling and Control, 11(3), 217–226. doi:10.15388/NA.2006.11.3.14743

22. Gautam, A. K., Verma, A. K., Bhattacharyya, K., & Banerjee, A. (2020). *Soret and Dufour effects on MHD boundary layer flow of non-Newtonian Carreau fluid with mixed convective heat and mass transfer over a moving plate*, Pramana–J. Phys. 94(108), https://doi.org/10.1007/s12043-020-01984-z

23. Srinivasacharya, D., Mendu, U., & Venumadhav, K. (2015). *MHD boundary layer flow of a nanofluid past a wedge*, Procedia Engineering, 127, 1064–1070.

24. Ariel, P.D. (1994). 94:108 *On hydromagnetic flow in a diverging channel*, Journal of Engineering Mathematics, 28, 415–428. DOI: 10.1007/BF00051275

Vanaja K.,
Department of Mathematics,
Malla Reddy University, Hyderabad,
India - 500100.
E-mail address: kourlavanaja24@gmail.com

and

Chenna Sumalatha,
Department of Mathematics,
Malla Reddy University, Hyderabad,
India - 500100.
E-mail address: sumalatha.chenna@gmail.com